

MATERIALS SCIENCE

Scalable microresonators for room-temperature detection of electron spin resonance from dilute, sub-nanoliter volume solids

Nandita Abhyankar^{1,2*}, Amit Agrawal^{1,2}, Pragma Shrestha^{2,3}, Russell Maier², Robert D. McMichael², Jason Campbell², Veronika Szalai^{2*}

We report a microresonator platform that allows room temperature detection of electron spins in volumes on the order of 100 pl, and demonstrate its utility to study low levels of dopants in perovskite oxides. We exploit the toroidal moment in a planar anapole, using a single unit of an anapole metamaterial architecture to produce a microwave resonance exhibiting a spatially confined magnetic field hotspot and simultaneously high quality-factor (*Q*-factor). To demonstrate the broad implementability of this design and its scalability to higher frequencies, we deploy the microresonators in a commercial electron paramagnetic resonance (EPR) spectrometer operating at 10 GHz and a NIST-built EPR spectrometer operating at 35 GHz. We report continuous-wave (CW) EPR spectra for various samples, including a dilute Mn²⁺-doped perovskite oxide, CaTiO₃, and a transition metal complex, CuCl₂·2H₂O. The anapole microresonator presented here is expected to enable multifrequency EPR characterization of dopants and defects in perovskite oxide microcrystals and other volume-limited materials of technological importance.

INTRODUCTION

Spin detection in volume-limited samples has applications in fields ranging from solid-state physics to structural biology (1–4). Magnetic resonance spectroscopies based on inductive detection are powerful and versatile techniques that can provide atomic-level structural and functional information for a wide range of samples under broadly variable conditions. However, conventional instrumentation is not sensitive enough to detect a large fraction of relevant volume-limited samples (<10 pl), which are often dilute doped samples with broad lines and concentrations <1 mole percent (mol %), resulting in fewer than 10⁸ spins per picoliter. For example, electron paramagnetic resonance (EPR) spectroscopy is a widely used technique to characterize atomic environments of dopants and defects in technologically relevant materials, which are often studied in their polycrystalline form because of the difficulty of growing single crystals. Single crystallites of perovskite oxides typically have micro- to nanoscale dimensions and volumes ranging from pico- to nanoliters (5). The perovskite complex oxide has a crystal structure that, due to its chemical tunability, is suited for a wide variety of technical and multifunctional applications (6). Depending on a number of crystal chemistry considerations that include but are not limited to stoichiometry, layering, cation ordering, and defect chemistry, the material can be designed for piezoelectric, insulating, catalytic, superconducting, and capacitive uses (7–10). Simple perovskite chemistries like SrTiO₃ or CaTiO₃ have limited use in commercial applications; however, these compositions serve as important model systems in which a multitude of fundamental studies are conducted (11–13). The study of point defects in these model systems helps facilitate metrology of defect chemistry in a broad range of technical ceramics.

The defect chemistry of a material can have a controlling effect on its resulting functional properties (14). The use of single crystals in EPR spectroscopy can yield orientational dependences of spin Hamiltonian parameters, allowing characterization of the substitutional properties of dopants (15). Rigorous characterization of the site of substitution, valence state, and nature of defect complex formation is necessary to explain the effect of a dopant ion on the resulting physical properties of a material (16–19). Critical information about anisotropies is masked by the superposition of EPR spectra from a distribution of orientations in polycrystalline materials. Despite the clear advantage of studying single crystals, sufficiently large (several microliters for conventional resonators) single crystals of dilute doped oxides are difficult to synthesize. Typical crystallite volumes are smaller than 1 pl, often approaching only 1 fl (5). To conduct routine inductive-detection EPR spectroscopy on single microcrystals of dilute doped oxides with sub-nanoliter volumes, it is necessary to develop resonators that have active volumes approaching 1 pl. These resonators must couple easily to microwave feedlines and must be scalable to higher frequencies. It is also advantageous if they can be deployed in various spectrometers without the need for customized hardware. We note that alternate spin detection techniques can provide ultrahigh sensitivities; for example, pulsed electrically detected magnetic resonance (20) can provide detection limits of a few hundred spins, while optically detected magnetic resonance (21) and magnetic resonance force microscopy (22, 23) can provide sensitivities down to the single-spin limit. However, these methods cannot provide the same depth of spectroscopic information provided by inductive-detection EPR spectroscopy. Sensitivities down to 1000 spins/√Hz have been reported for inductive detection using superconducting microresonators (4). However, these devices also require highly restrictive experimental conditions, including cryogenic temperatures, low magnetic fields, and exotic detection circuitry such as Josephson parametric amplifiers. Given that existing instrumentation in many laboratories relies on spectrometers built to measure spins using inductive detection, increasing the

Copyright © 2020
The Authors, some
rights reserved;
exclusive licensee
American Association
for the Advancement
of Science. No claim to
original U.S. Government
Works. Distributed
under a Creative
Commons Attribution
NonCommercial
License 4.0 (CC BY-NC).

¹Institute for Research in Electronics and Applied Physics, University of Maryland, College Park, MD 20742, USA. ²National Institute of Standards and Technology, Gaithersburg, MD 20899, USA. ³Theiss Research, La Jolla, CA 92037, USA.

*Corresponding author. Email: veronika.szalai@nist.gov (V.S.); nandita.abhyankar@nist.gov (N.A.)

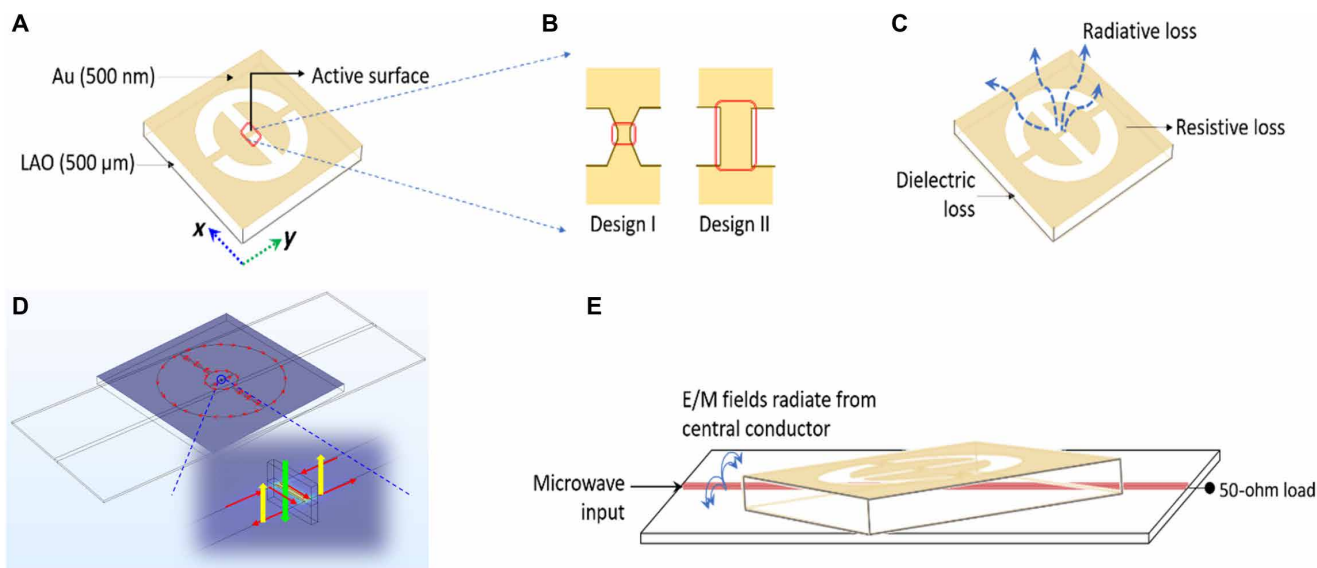


Fig. 1. Overview of planar inverse anapole microresonators. (A) Schematic of the planar inverse anapole resonator composed of a dielectric substrate whose top surface is coated with a gold film. The red highlighted region is the active region of the microresonator, where the microwave magnetic field is concentrated around the central bridge. (B) Two designs of the central bridge. (C) Types of power losses occurring from planar microresonators (described in text below). (D) Schematic of currents (red arrows) and dipoles in the microstrip-microresonator device. The zoomed region shows the bridge, where B_1 is concentrated. Red arrows indicate the directions of currents flowing through and adjacent to the central bridge. Current through the bridge results in a magnetic dipole in/out of the resonator plane (green arrow). The currents flowing through the etched metallic region adjacent to the bridge result in a degenerate toroidal moment, also directed in/out of the plane (yellow arrows). (E) Schematic of the microresonator coupled to the electromagnetic (E/M) fields radiating from the central conductor of the microstrip.

sensitivity of inductive detection for a broad range of experimental conditions extends the power of magnetic resonance spectroscopies to nanoscale samples. Here, we report a novel microresonator design for EPR spectroscopy, which uses a single unit of a planar anapole metamaterial architecture exhibiting toroidal moment to increase the quality-factor (Q -factor) while simultaneously confining the spatial extent of the electromagnetic field (Fig. 1) (24). We exploit the duality of electric and magnetic fields—predicted by Babinet’s principle—to design an inverse architecture that efficiently confines microwave magnetic fields within a picoliter-scale volume at the center of the resonator (25–27). Babinet’s principle has been previously used in the design of complementary pairs of resonant structures in which the “inverted” counterpart shows complementary magnetic/electric near-field distributions compared to the original structure. We provide experimental verification of the active volume of these “planar inverse anapole” microresonators, which simultaneously exhibit high Q -factors and have a geometry that allows easy coupling to an external microwave feedline. We have deployed these microresonators in a Bruker E580 EPR spectrometer operating at 10 GHz and a National Institute of Standards and Technology (NIST)–built EPR spectrometer operating at 35 GHz to obtain room temperature continuous-wave (CW) EPR spectra of various materials, including a dilute (<0.05 mol %) Mn^{2+} -doped sample of $CaTiO_3$ and a transition metal complex, $CuCl_2 \cdot 2H_2O$.

Compared to conventional cavities, miniaturized active volumes offer a path toward improved detection limits. Nonresonant scanning probes and microresonators have been designed and demonstrated as planar metallic structures patterned on dielectric substrates (4, 28–35). These structures can be readily fabricated using standard photolithographic techniques, yielding nanoliter active volumes in micrometer-scale resonators. The effect of this miniaturization on

sensitivity can be explained in terms of two main resonator characteristics: the filling factor and the quality factor (Q -factor) (30, 33, 36–38). The filling factor can be roughly described as the fraction of the active volume of the resonator to the volume occupied by the sample (see the “Sensitivity Analysis” section in the Supplementary Materials for a quantitative description of filling factor, Q -factor, and signal gain as a function of filling factor and Q -factor). When the active volume becomes comparable to the sample volume, there is a gain of several orders of magnitude in the filling factor (compared to conventional cavity resonators) and a corresponding gain in absolute sensitivity.

On the other hand, miniaturization typically deteriorates the Q -factor, which is a measure of how well the resonator retains the energy coupled from the microwave source. Compared to cavity resonators, power losses are higher in open resonant structures such as loop-gap resonators and microstrip-based structures (39, 40). The lossy nature of microresonators increases the difficulty of coupling with a microwave source such as a microstrip. In addition, the size mismatch between microresonators and microstrips results in further inefficiency of coupling. Thus, a decrease in Q -factor deteriorates both absolute sensitivity and concentration sensitivity. To increase the Q -factor, power losses must be decreased (Fig. 1C). The Q -factor is dependent on the combination of three types of losses: dielectric losses from the substrate, conductive losses from the metal, and radiative losses from the microstrip structure. Dielectric power loss is inversely proportional to the loss tangent of the substrate (41) and can be decreased using a low-loss dielectric substrate (32, 33). Resistive power loss can be decreased by operating at lower temperatures, which is a commonly adopted strategy to increase Q -factors of small-volume planar resonators (4, 34, 35). Here, we minimize radiative loss to increase the Q -factor of microresonators at room

temperature while confining the microwave excitation field within a volume on the order of 100 pl or smaller. It should be noted that radiation shields can be used to decrease radiative losses from open resonant structures. This approach can provide Q -factor improvements of up to 50% (42–44). In comparison, the microresonator design reported here decreases radiation losses intrinsic to the resonator, improving the Q -factor by an order of magnitude compared to microresonators reported previously. Using this approach, we report an upper spin detection limit of $(7 \pm 2 \times 10^5)/\text{mT}\sqrt{\text{Hz}}$ in a volume of approximately 100 pl at room temperature. The sensitivity gains at lower temperatures are expected to be correspondingly higher.

The reduction in radiation losses, resulting in high Q -factors of anapole resonators, is due to diminished far-field radiation because of destructive interference between toroidal and electrical dipole moments (24, 45–49). Arrays of such resonators with toroidal moments can produce Q -factors as high as 10^5 (24). This approach cannot be directly applied to resonators for EPR spectroscopy because of the following additional considerations: (i) For sensitive measurements of the reflected power, the resonator must be critically coupled to a microwave source; (ii) there must be a sample volume where the microwave magnetic field B_1 is perpendicular to the static magnetic field B_0 (for perpendicular mode measurements); and (iii) the microwave electric field must be minimized in the active volume to avoid dielectric losses from lossy samples such as aqueous solutions. With these considerations in mind, our design uses a complementary or inverse anapole structure. Previously investigated anapole resonators typically feature mostly bare substrates with regions of patterned metals and microscale gaps where the electric field is concentrated. In contrast, we exploited the duality of electric and magnetic fields to design an inverse, mostly metallized structure with a central bridging strip that supports a magnetic field “hotspot” at the center of the resonator (Fig. 1A). We have simulated both anapole and inverse anapole resonators to verify their complementarity (see fig. S1). In the case of a regular anapole design (as reported by Basharin *et al.*, for example), (24) the electric dipole is formed in the central gap in the split ring, and the resulting circulating magnetic field (in the air gaps) generates the toroidal moment that is anti-parallel to the electric dipole. In the complementary or inverse architecture, an in/out-of-plane magnetic dipole forms around the top and bottom of the central metal notch (the short). On the other hand, the electrical field-driven circulating currents around the etched parts result in a net toroidal moment that is also in/out of plane—anti-parallel and degenerate with the magnetic dipole. A simplified picture of the current flow on the resonator surface is shown in Fig. 1D. The current distribution in the microstrip-microresonator device is more complicated (see fig. S2). In the ideal inverted structure, the metal plane should be infinite, while in the resonator, it is truncated at the edges. We conducted simulations to test the effect of this truncation on the inverse anapole mode (see table S1). Increasing the outer length of the metal rectangle from 12 to 15 mm changes the resonant frequency and loss factor (imaginary component of eigenmode) by less than 10%. We surmise that the structure approximates an ideal inverted structure for two reasons: (i) Fringing fields from the microstrip extend for a length much smaller than the length of the microresonator (see fig. S3), and (ii) the outer length of the metal layer is much larger than the coupling structure (the capacitive gaps) and the central bridge.

This structure was fabricated on a low-loss dielectric [either lanthanum aluminate (LAO) or lanthanum strontium titanate (LSAT)] to

minimize dielectric losses from the resonator (32, 33). The dielectric permittivities of LAO and LSAT vary in the ranges of 23.6 to 24.0 and 22.7 to 22.9, respectively, in the temperature range of 2 to 300 K (50, 51). In this temperature range, the loss tangents of LAO and LSAT vary in the ranges of 1×10^{-6} to 2×10^{-5} and 1×10^{-4} to 6×10^{-4} , respectively. Finite element simulations indicate that the variation in dielectric permittivity is expected to result in a variation of <0.5 GHz in the resonance frequency of the device, shifting it from 9.7 to 9.3 GHz. The observed frequency varies in the range of 9.2 to 9.8 GHz, depending on the x position of the microresonator on the microstrip so that the decrease in frequency caused by low temperature may be compensated for by changing the position of the microresonator on the microstrip.

We made microresonators with two types of bridges (Fig. 1B): in design I, the bridge is cinched at the center to obtain a smaller active surface, and in design II, the bridge is a straight line that results in a large active surface. Smaller active volumes and active heights are advantageous for samples such as microcrystals or thin films, in which it is desirable to restrict the microwave power to the epitaxial film so that it can be selectively probed without interference from the substrate. Here, we report the use of design I for demonstration at 10 GHz and design II at 35 GHz. This choice was arbitrary because either design can be applied at either frequency. We merely wanted to demonstrate the functionality of both designs.

Lack of scalability to higher frequencies is one of the challenges in microresonator design. Higher-frequency EPR studies can provide greater sensitivity and resolution, potentially providing spectral information not available at lower frequencies. In addition, multi-frequency EPR can be used to separate field-dependent and field-independent components of the EPR spectrum. However, most reported microresonator designs, such as those based on loop-gap architectures, become impractically small at higher frequencies. In contrast, the large overall size of the planar inverse anapole resonator enables scaling to higher frequencies without sacrificing the active volume or ease of coupling to a microwave source. Thus, this design overcomes the challenges of ring or loop-gap microresonators, which become difficult to fabricate and to couple to microwave sources owing to progressively small radii with increasing frequency. The scalability of the anapole architecture can enable high-frequency EPR studies for volume-limited samples.

In both bridge designs, the microwave magnetic field B_1 is concentrated in a small volume around the central bridge and is directed perpendicular to the flow of current (zoom inset in Fig. 1D). Below, we show that the experimental Q -factors for these structures are in the approximate range of 250 to 350 at both 10 and 35 GHz. Important advantages of this design include active volumes smaller than 100 pl, ease of coupling to a microwave feedline, and scalability to higher frequencies. Last, we demonstrate that these devices can be integrated into existing EPR spectrometers for wide implementability.

RESULTS AND DISCUSSION

All resonators were fabricated by patterning gold films of thickness 500 nm on either LAO or LSAT substrates (dielectric constants ranging from 22 to 25) with thicknesses of 500 μm . The complete fabrication protocol is provided in Materials and Methods. Simulations of field distributions of the devices were conducted using the commercial finite element analysis software COMSOL. The complete finite element model of the planar inverse anapole resonator

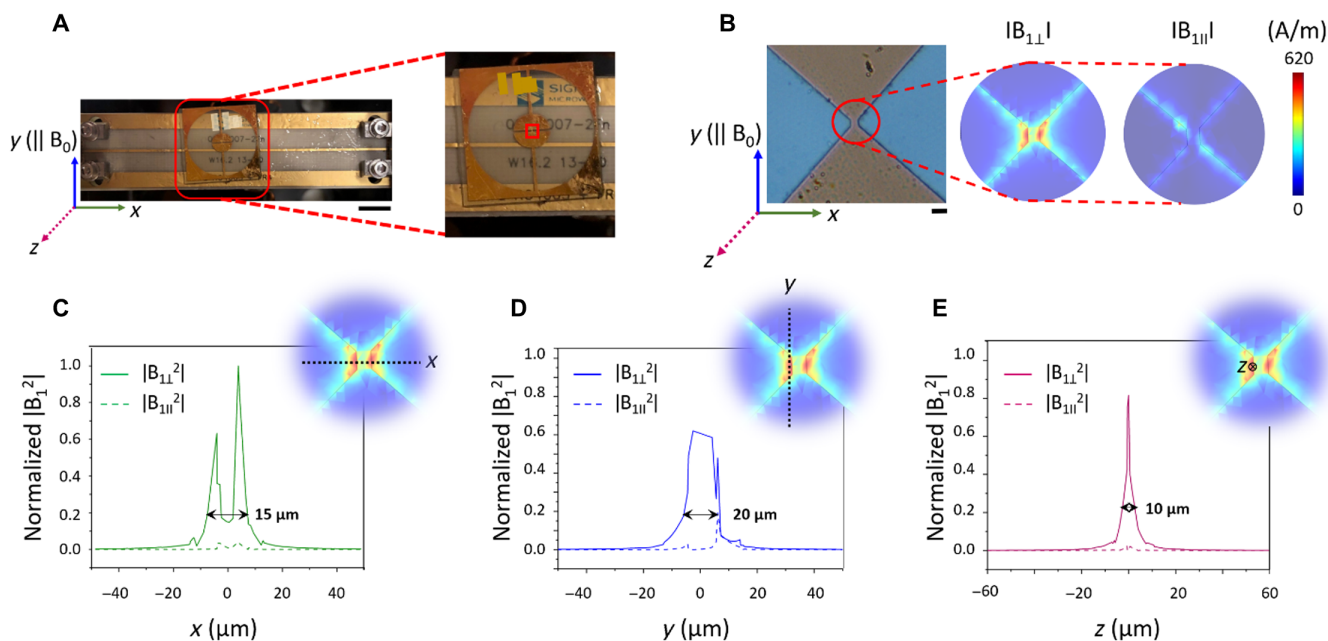


Fig. 2. A 10-GHz device and finite element simulation of active volume. (A) Top view of a microresonator-microstrip device with an experimental resonant frequency of 9.7 GHz. Scale bar, 5 mm. The zoomed region in the panel on the right shows the microresonator chip. The red outline at the center of the right panel encloses the active region of the resonator (photo credit: Nandita Abhyankar, NIST). (B) The left panel shows a zoomed-in optical micrograph of the active region (design I) of the microresonator. Scale bar, 10 μm . The panels to the right of the optical micrograph show simulated distributions of perpendicular ($B_{1\perp}$) and tangential ($B_{1\parallel}$) components of the microwave magnetic field B_1 in the x - y plane, showing the central $B_{1\perp}$ hotspot. (C to E) Normalized absolute values of simulated $B_{1\perp}^2$ (solid lines) and $B_{1\parallel}^2$ (dashed lines) along the x , y , and z coordinates. The black dotted lines in the insets are the cut lines along which the field is plotted (z is perpendicular to the plane of the resonator). An input voltage of 1 V and impedance of 50 ohms was set in the finite element simulations, resulting in an input power of 20 mW.

with dimensions is shown in fig. S4. Figure S5 provides dimensions of features of the metallized layer.

Simulation and experimental verification of the active volume

Figure 2A shows a device consisting of the planar inverse anapole microresonator coupled to a microstrip (which is further connected to the microwave bridge via a coaxial cable, not shown in the figure). The resonator was designed to exhibit a high- Q anapole mode at 10 GHz. The left panel of Fig. 2B shows a micrograph of the active region of the microresonator based on design I, while the right panel shows finite element simulations of the distribution of the perpendicular ($B_{1\perp}$) and tangential ($B_{1\parallel}$) components of the microwave magnetic field in the active region. $B_{1\perp}$ is the sum of components of B_1 that are perpendicular to the static magnetic field B_0 . Here, $B_{1\perp}$ is designated as the absolute value of $\sqrt{(B_{1x}^2 + B_{1z}^2)}$, with B_0 applied along the y axis. Thus, $\sqrt{B_{1y}^2}$ is the absolute value of the tangential component of the microwave magnetic field. The EPR signal is directly proportional to $B_{1\perp}^2$. Figure S6 shows that the electric field is concentrated at the edges of the capacitive gaps and is well separated from the active region at the center of the resonator. This separation of electric and magnetic fields is particularly advantageous for samples with high dielectric losses.

The patterned gold film converges on the small central bridge of design I, with an area of approximately $(5 \times 5) \mu\text{m}^2$. Figure 2 (C to E) shows plots of the simulated $B_{1\perp}^2$ and $B_{1\parallel}^2$ in the x , y , and z directions, respectively, normalized to the highest value of $B_{1\perp}^2$. The dotted lines in the insets are the cut lines along which $B_{1\perp}^2$ and $B_{1\parallel}^2$ are plotted. They were chosen to cut through the region of strongest B_1

in the plane of the resonator. These distributions indicate that $B_{1\perp}^2$ drops by 80% from its maximum value outside a volume of $(15 \mu\text{m} \text{ by } 20 \mu\text{m} \text{ by } 5 \mu\text{m})$ around the central bridge, i.e., approximately $1500 \mu\text{m}^3$ or 1.5 pL. The dimension in the z direction is halved because only the volume above the resonator surface is available for sample placement. The tangential component of B_1^2 , i.e., $B_{1\parallel}^2$, is also plotted in Fig. 2 (C to E) and comprises less than 5% of the total B_1^2 . Table 1 shows the calculated mode volumes for the two different bridge designs at two different frequencies. In Fig. 3 below, we show that mode volumes are not an accurate representation of the volume responsible for most of the signal in an open resonant structure such as a microstrip resonator. The calculated mode volumes are much higher than the estimated active volume, and we show in Fig. 3 that most of the signal does originate from a much smaller active volume at the center of the microresonator.

The trends in simulations of field distributions were verified by simulating and observing the loss in signal when a sample is moved away from the active region (Fig. 3). A single crystal of the α, γ -bis-diphenylene- β -phenylallyl (BDPA)-benzene complex was placed on the B_1 hotspot and then moved away by a small increment along the x axis. The crystal had a volume of about 70 pL and covered an area much larger than the active area of the resonator. Figure 3A shows the active region of the microresonator surface with no sample on it. Figure 3 (B and C) shows the sample at two different positions separated in x by $7 \pm 3 \mu\text{m}$. The BDPA-benzene crystal was chosen because it has a strong and narrow signal that is easy to quantify. On the basis of the large extent of the BDPA-benzene microcrystal compared to the size of the active region, the reduction in signal intensity going from Fig. 3B to Fig. 3C is attributed

Table 1. Resonator parameters obtained from simulations and experiment.

	Design I, 10 GHz	Design II, 10 GHz	Design I, 35 GHz	Design II, 35 GHz
ν_{res}	9.3–9.8 GHz	9.3–9.8 GHz	34.7–35 GHz	34.7–35 GHz
Q (simulation)	220 ± 20	200 ± 20	580 ± 30	760 ± 50
Q (experiment)	250 ± 50	–	–	250 ± 50
Conversion efficiency (simulation)	3 ± 0.4 mT/√W	9 ± 1 mT/√W	11 ± 2 mT/√W	3 ± 0.3 mT/√W
Conversion efficiency (experiment)	3 ± 0.3 mT/√W	–	–	6 ± 1 mT/√W
$P_{1/2}$ (experiment)	0.025 ± 0.05 mW	–	–	Lower than lowest available power
Mode volume (simulation)*	30 nl	3 nl	400 pl	4 nl

*Mode volume was calculated on the basis of the filling factor of a small volume in the active region of the microresonator, using the following formula (57):

$$\text{Mode volume} = \text{Small volume} \times \frac{\int_{\text{resonator}} B_{1\perp}^2 dV}{\int_{\text{small volume}} B_{1\perp}^2 dV}$$

solely to the change in amount of sample occupying the resonator active volume. In Fig. 3B, the entire active volume is occupied by the BDPA-benzene crystal. Moving the crystal $7 \pm 3 \mu\text{m}$ away from the active region causes the signal intensity to decrease by 75%, as seen from the CW EPR spectra in Fig. 3D. Because the y and z dimensions are also much larger than the simulated dimensions of the active volume, this reduction in signal intensity can be used to directly estimate the active range along the x axis. Assuming an equal range on both sides of the active surface, the active range along the x axis is estimated to be $20 \mu\text{m}$, which is comparable to the active range indicated by Fig. 2C. Figure 3E shows the power-saturation curves with the BDPA-benzene single crystal in positions Fig. 3B and Fig. 3C. Figure 3F shows that the ratio of double-integrated signals from Fig. 3B and Fig. 3C reaches a constant value upon saturation. These results suggest that even if a large sample is placed on the hotspot, most of the signal originates from a small volume around the central bridge. To estimate the volume responsible for a majority of the signal from a large sample, we used finite element simulations to obtain the integral of $B_{1\perp}^2$ over a large sample, and over smaller sub-volumes at the center of the sample. The field inhomogeneity in planar microresonators makes it difficult to estimate their active volume. For example, Fig. 3H shows that a volume of approximately 2 pl around the central bridge shown in Fig. 3A accounts for 20% of the total integrated $B_{1\perp}^2$ over a large sample. A volume of approximately 25 pl accounts for 55% of the integrated $B_{1\perp}^2$ while a volume of approximately 50 pl accounts for 65% of the total integrated $B_{1\perp}^2$ over a large sample. This weighted distribution of $B_{1\perp}^2$ is graphically represented in Fig. 3G. The mode volumes calculated in Table 1 are much higher than the “active volume” of approximately 50 to 100 pl estimated from Fig. 3G. This discrepancy can be explained by taking into account the high B_1 inhomogeneity and diffuse nature of B_1 distribution on the resonator surface.

Figure 3E shows the power saturation curves of the BDPA-benzene single crystal placed at positions shown in Fig. 3B and Fig. 3C. The error bars represent a single SD in double-integrated area, due to random noise of the EPR spectrum. Crystalline BDPA saturates at a B_1 value of 0.03 mT [based on (52) and assuming a conversion factor of approximately 0.1 mT/√W for a rectangular cavity with a

Q -factor of approximately 3000]. The power saturation curves were fit to an asymptotic growth function, and the saturation power was defined as that at which the saturation curve deviates from linearity (see fig. S7A). By this analysis, the power-to-field conversion efficiency for the microresonator-microstrip device (Fig. 4) used in Figs. 2 and 3 was found to be $(3 \pm 0.5) \text{ mT}/\sqrt{\text{W}}$. The error represents a single SD due to uncertainty in the power corresponding to saturation. The simulated value of the conversion efficiency, based on the highest value of $B_{1\perp}$ in the model, is $(3 \pm 0.4) \text{ mT}/\sqrt{\text{W}}$ (see Table 1). These values appear to be low for the active volume in consideration and are comparable at 10 and 35 GHz. The conversion efficiency is calculated for the entire microstrip-microresonator device on the basis of the nominal output power of the bridge. In reality, only a small fraction of this power is ultimately coupled into the microresonator. Second, while the active volume is on the order of 50 to 100 pl, it is much smaller than the outer dimensions of the resonator. Thus, a decrease in overall size of the resonator is not expected to have a substantial effect on the filling factor or conversion efficiency. While there appears to be a reasonable correspondence between the experimental and simulated conversion efficiencies of the microstrip-microresonator devices, there are many parameters that affect the coupling between the microresonator and microstrip and hence can be used to tune the conversion efficiency. These are discussed in the next section.

This experimental conversion efficiency does not account for the $B_{1\perp}$ inhomogeneity in the active region, which can be disadvantageous for pulse measurements. An estimate of the B_1 homogeneity can be obtained from the power saturation curve using equation 7 from (53). This analysis of the power saturation data in Fig. 3 resulted in a value of $\mathcal{E} = 0.5 \pm 0.1$, indicating highly inhomogeneous saturation. The fit is presented in fig. S7B.

Coupling and tuning

An advantage of the planar inverse anapole resonator is that its overall large size allows easy coupling to an external microwave feedline. Figure 4A shows a microresonator-microstrip device operating at 9.75 GHz. The microresonator is adhered to a commercial RO4003 microstrip using a small amount of silicone grease. The position of the microresonator relative to the central conductor of the microstrip

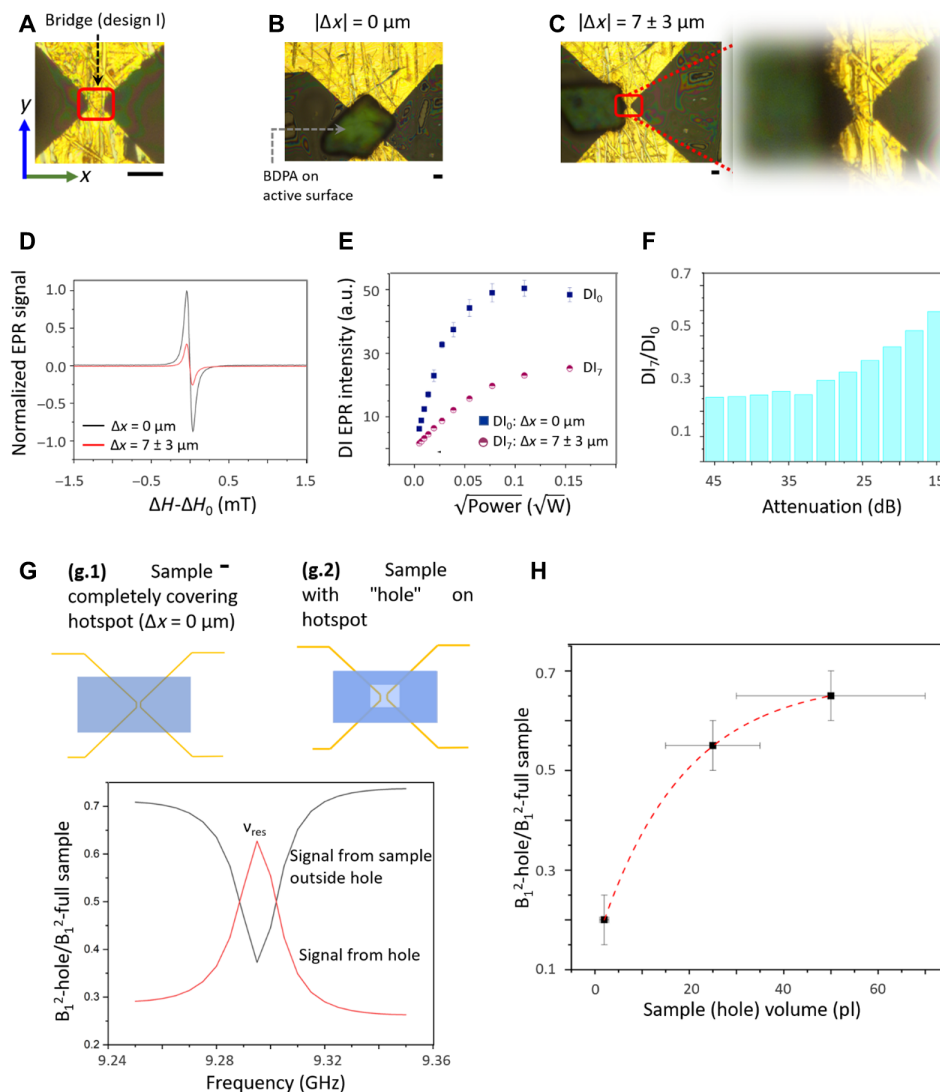


Fig. 3. Experimental demonstration of active volume for 10-GHz microresonator. (A) Optical micrograph of a 10-GHz microresonator with the active region based on design I. (B and C) Optical micrographs of a BDPA-benzene crystal (approximately $50\ \mu\text{m}$ by $90\ \mu\text{m}$ by $15\ \mu\text{m}$) placed over the active surface (B) and $7 \pm 3\ \mu\text{m}$ away from the active surface (C). Scale bars in (A) to (C) and (G) represent $10\ \mu\text{m}$, and the width of the central bridge is $5\ \mu\text{m}$. (D) Comparison of EPR spectra obtained from (B) and (C) at approximately $20\text{-}\mu\text{W}$ applied power and normalized to the maximum signal intensity obtained from (B). (E) Comparison of power saturation curves, i.e., plots of double-integrated (DI) signal intensity versus square root of power in positions (B) and (C) (a.u., arbitrary units). The maximum power output of the Bruker bridge is $158\ \text{mW}$. The error bars represent a single SD in double-integrated area due to random noise of the EPR spectrum. (F) Ratio of double-integrated signal intensities in positions (B) and (C) as a function of attenuation. (G) Simulation of loss of signal in sample excluding the active volume (hole) of $60 \times 60 \times 15\ \mu\text{m}^3$, when compared to volume including active volume. (H) Normalized volume-integrals of $B_{1\perp}^2$ as a function of selected sample volume. As the sample radiates outwards from the central bridge, its weighted contribution to the signal decreases.

is defined in terms of three parameters: x (distance along the central conductor of the microstrip), y (vertical offset from the central conductor), and θ (angle between the central conductor and capacitive gaps of the microresonator). The parameters y and θ can be used to control the coupling between the microstrip and the microresonator (Fig. 4B). The photographs in Fig. 4C show the relative positions of the microresonator with respect to the microstrip in the critically coupled and uncoupled states. Also shown are the experimental plots of the reflection coefficient (S_{11}) versus frequency in the critically coupled and uncoupled states, showing a resonance frequency of $9.75\ \text{GHz}$ for the critically coupled device. The linewidth at 3 dB below the baseline is typically used as an estimate of

the Q -factor. Therefore, it is important to establish the baseline by comparing S_{11} profiles of the coupled and uncoupled devices. Using these data, the experimental Q -factor is estimated to be 250 ± 50 at room temperature. The error is a single SD due to variability in coupling of the microresonator and microstrip. Because we have used low-loss dielectric substrates such as those used in previous reports (33), we attribute this improvement in Q -factor at room temperature to the diminished radiation losses provided by the inverse anapole mode. This improvement is obtained while confining B_1 to a volume on the order of $100\ \text{pl}$. Basharin *et al.* (24) report Q -factors in the range of 10^4 to 10^5 for arrays of coupled resonators in the metamaterial. However, the microresonator in the present report is

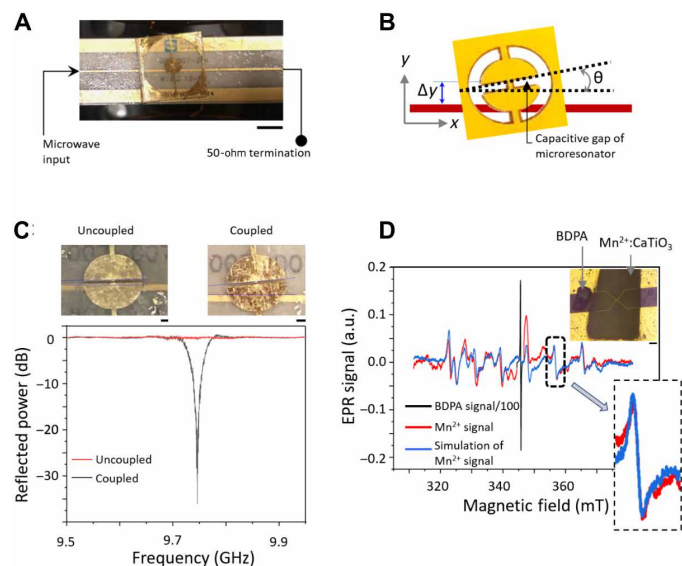


Fig. 4. Microresonator-microstrip coupling. (A) A 10-GHz microresonator-microstrip device that replaces the resonator in a Bruker E580 EPR spectrometer. Scale bar, 5 mm. (B) Cartoon representation of the device, showing the position parameters that can be used to control coupling. The blue double-headed arrow indicates the y -offset of the resonator center from the central conductor of the microstrip. (C) Photographs show the microresonator position in the uncoupled and critically coupled states (dashed blue lines are visual aids to demarcate the tops of the microstrip and capacitive gap of the microresonator). Both scale bars represent 0.5 mm. The red and black lines are the plots of reflected power versus frequency for the uncoupled state and critically coupled state, respectively, after background subtraction. (D) Simulated (blue) and experimental (red, black) CW EPR spectra of 0.05 mol % Mn^{2+} -doped CaTiO_3 . The sharp black line at the center is the signal from the BDPA microcrystal used for modulation coil calibration. The BDPA signal has been adjusted to make it visually comparable to the Mn^{2+} signal. The experimental spectrum was obtained using the coupled microresonator-microstrip device from (C). The inset optical micrograph shows the single micro-particle placed over the microresonator. The dashed yellow lines are visual aids showing the edges of the microresonator below the sample. The SNR of the component highlighted in the dashed box was used for sensitivity calculations, as explained in the text (photo credits: Nandita Abhyankar, NIST).

a unit of the metamaterial array and therefore intrinsically has a lower Q -factor compared to an array. Second, the thin metal layer deposited on a dielectric substrate results in additional losses compared to purely metallic arrays. These factors combine to yield Q -factors that are much smaller than those observed by Basharin *et al.* (24). We observed that the resonant frequency of the microresonator-microstrip device can be varied simply by changing the position of the microresonator on the microstrip (fig. S8). This method provides a tunability of approximately 500 MHz at both 10 and 35 GHz. Because of the complex structure of the device, a model of the coupling between microresonator and microstrip is beyond the scope of this paper. Figures S8 and S9 provide a detailed phenomenological description of the dependence of device frequency and coupling on x , y , and θ .

Testing microresonator sensitivity at room temperature

We tested the sensitivity of the planar inverse anapole microresonator by obtaining EPR spectra of a dilute (0.05 mol %) Mn^{2+} -doped sample of CaTiO_3 (inset of Fig. 4D), using the critically coupled device with a resonance frequency of 9.75 GHz. A crystal of BDPA-benzene

complex was used to calibrate modulation coil settings in the Bruker EPR software Xepr. Currently, single-crystal data for dilute perovskite oxide single crystals are difficult to obtain because (i) the commercial availability of doped single crystals is limited, (ii) a high amount of expertise is required to grow single-crystal perovskites, (iii) high-quality single crystals grown from conventional melt processes exhibit inhomogeneities, and (iv) nonconventional growth techniques result in crystallite volumes that are typically smaller than 1 μl and often closer to 1 fl (54). Therefore, in conventional EPR spectrometers, novel perovskite chemistries can only be measured in their polycrystalline form, usually as compressed pellets consisting of thousands of microparticles, with a total volume of several microliters. To test the upper limit of detection of the microresonator, we picked out a microparticle with a total volume of approximately 5 nl (Fig. 4D). The finite element simulations detailed in Fig. 3 suggest that only 50 ± 20 pl of this large volume is probed by the microresonator. We use this simulated “active volume” to estimate the upper limit of detection, although further corroboration is required using a smaller crystal with a volume approaching 1 pl. We anticipate that further refinements in the detection circuitry will allow us to increase the power incident on the microresonator, resulting in proportionate improvements in volume-sensitivity. To estimate the sensitivity, we chose the signal enclosed in the dashed outline in Fig. 4D because it is clearly identifiable and its linewidth and peak-to-peak signal intensity can be determined with reasonable certainty. The data shown in Fig. 4D were obtained with a power output of 158 mW from the Bruker bridge. As noted in the discussion of conversion efficiency above, the actual power incident on the microresonator is a small fraction of the power entering the microstrip. The total spin density for this sample is approximately $9 \times 10^{18}/\text{ml}$ [sample “0.05Mn” from (55)]. Therefore, the total number of Mn^{2+} spins in the active volume of 50 ± 20 pl is approximately 5×10^{11} . The number of spins contributing to the chosen line was calculated from the ratio of its double-integrated intensity to the double-integrated intensity of the complete spectrum, excluding the BDPA signal. This ratio was found to be $(10 \pm 2)\%$, leading to a spin count of 5×10^{10} spins for the chosen line. The error is a single SD due to uncertainty in observed linewidth. In previous reports, the sensitivity is normalized per unit signal-to-noise ratio (SNR), linewidth, and square root of the detection bandwidth (4, 30–35). In the present case, these numbers are 25, 0.8 mT, and $0.7 \sqrt{\text{Hz}}$ (Materials and Methods), respectively. Using these values and the previous sensitivity calculation approach, our demonstrated upper limit of detection is

$$\frac{5 \times 10^{10}}{25 \times 0.8 \times 0.7} = (4 \pm 1) \times 10^9 / \text{mT} \sqrt{\text{Hz}}$$

If the sensitivity is calculated on the basis of the method used in (35), the total linewidth for the spectrum would be approximately 40 mT. Therefore, the calculated upper limit of detection, normalized to the linewidth (40 mT), bandwidth ($0.7 \sqrt{\text{Hz}}$), and SNR (25), is

$$\frac{5 \times 10^{11}}{25 \times 40 \times 0.7} = (7 \pm 2) \times 10^8 / \text{mT} \sqrt{\text{Hz}}$$

The data were obtained by integrating our devices into standard operational EPR spectrometers. We anticipate that further refinements in the detection circuitry will allow us to increase the power incident on the microresonator and will result in further improvements in volume sensitivity.

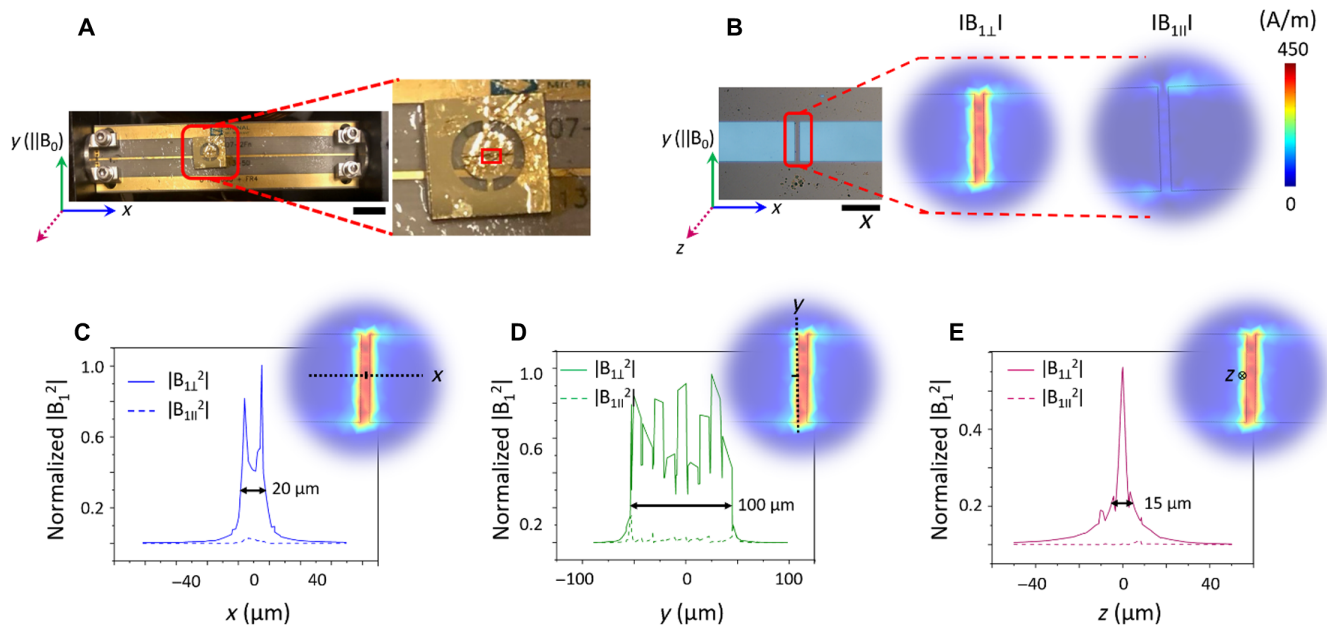


Fig. 5. A 35-GHz device and simulation of active volume. (A) Planar inverse anapole microresonator-microstrip device operating at 35 GHz. The zoomed-in region on the right shows the microresonator chip (the red outline encloses the active region) (photo credit: Nandita Abhyankar, NIST). (B) Optical micrograph of the active region. The right panel shows the simulated distributions of the absolute values of perpendicular and tangential components of B_1 in the xy plane, showing the central B_1 hotspot in a small volume around the bridge. (C to E) Normalized absolute values of $B_{1\perp}^2$ and $B_{1\parallel}^2$ along the x , y , and z coordinates. An input voltage of 1 V and an impedance of 50 ohms, i.e., an input power of 20 mW, were set in the finite element simulations.

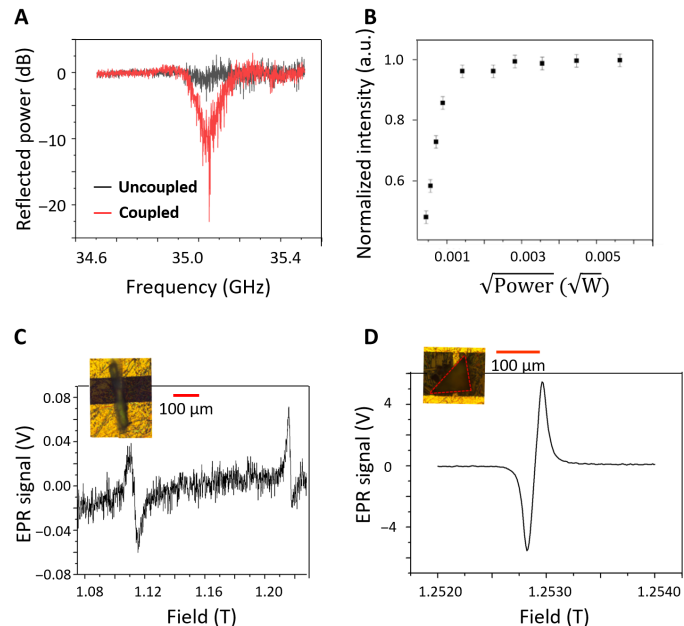


Fig. 6. Performance of the 35-GHz planar inverse anapole microresonator coupled to a microstrip. (A) Frequency profiles of reflection coefficient in the uncoupled (red) and critically coupled (black) states. (B) Power saturation curve for a BDPA-benzene single crystal. The error bars represent systematic uncertainty of a single SD in double-integrated area due to splitting of the EPR signal detected in the I/Q channels. (C) CW EPR spectrum of a microcrystal of $\text{CuCl}_2 \cdot 2\text{H}_2\text{O}$. (D) CW EPR spectrum of a microcrystal of BDPA-benzene complex. (Photo credits for (C) and (D): Nandita Abhyankar, NIST)

The experimental EPR spectrum was validated by simulations using isotropic Landé g -factor = 2.001, isotropic hyperfine splitting parameter $A = 239.3$ MHz, linewidth = 0.5 mT, and zero-field splitting parameters $D = 434$ MHz and $E = -41$ MHz. Random noise to produce an SNR of 25 was added to the simulated spectrum to match the SNR measured from experiment.

Scalability to higher frequencies

We report the first CW EPR spectra acquired from picoliter active volumes at 35 GHz. Figure 5A shows a microresonator-microstrip device operating at 35 GHz. Figure 5B shows an optical micrograph of the active region (outlined in red in Fig. 5A) based on design II. The area of the active surface is $\approx 1000 \mu\text{m}^2$. Figure 5 (C to E) shows the distribution of $B_{1\perp}$ along the x , y , and z directions, respectively.

As is the case at 10 GHz, the coupling of the 35 GHz microresonators is controlled via the y position and orientation θ of the microresonator relative to the central conductor of the microstrip. The frequency profiles of reflection coefficient in the coupled and uncoupled states are shown in Fig. 6A. The Q -factor of this microresonator-microstrip device is 250 ± 50 . The error is a single SD due to variability in coupling between the microresonator and microstrip. The power-to-field conversion ratio, determined from the power saturation curve for the BDPA-benzene complex, is $(7 \pm 1) \text{ mT} / \sqrt{\text{W}}$ (Fig. 6B). The error is a single SD due to uncertainty in measurement of the power at which the EPR signal saturates. The maximum power output of the NIST-built EPR spectrometer in CW mode is 200 mW.

Figure 6 (C and D) shows CW EPR spectra obtained from microcrystals of $\text{CuCl}_2 \cdot 2\text{H}_2\text{O}$ and crystalline BDPA-benzene complex,

respectively. The signal intensity for $\text{CuCl}_2 \cdot 2\text{H}_2\text{O}$ is limited by our maximum modulation amplitude of ≈ 0.1 mT (limited by spectrometer settings in the present case) compared to the linewidth of 5.5 mT. For $\text{CuCl}_2 \cdot 2\text{H}_2\text{O}$, the Landé g -factor, $[g_a g_b g_c] = [2.187 \ 2.037 \ 2.252]$, as reported in (44). We surmise that the two observed signals at 11.1 and 12.1 T are caused by crystal twinning. We have also obtained CW EPR spectra for a dilute (0.01 mol %) doped single crystal of $\text{Fe}^{3+}:\text{SrTiO}_3$ (see fig. S10). In our current configuration, we are unable to obtain a modulation amplitude of more than 1G with the microresonator setup. This limits the apparent sensitivity of the 35-GHz microstrip-microresonator devices, and hence, we have not estimated this quantity.

This is the first report of CW EPR spectra obtained from picoliter volumes at 35 GHz, owing to improved coupling provided by better Q -factors. These results demonstrate the scalability of the planar inverse anapole design to higher frequencies, which has previously been a major obstacle in the application of microresonators to higher-frequency EPR experiments.

CONCLUSIONS

In conclusion, we have demonstrated the use of a toroidal metamaterial unit to improve the Q -factors of EPR microresonators by an order of magnitude while confining the microwave magnetic field to picoliter volumes. The improvement in Q -factors enables CW EPR experiments by integration of microresonator-microstrip devices into standard operation EPR spectrometers. Experimental demonstration of the active volume is provided using CW EPR spectra of a strongly paramagnetic sample. The CW EPR spectrum obtained for a microparticle of <0.05 mol % $\text{Mn}^{2+}:\text{CaTiO}_3$ yields a calculated upper limit of detection of $(7 \pm 2 \times 10^8)/\text{mT}\sqrt{\text{Hz}}$. We anticipate that further refinement of the coupling apparatus and spectrometer setup will result in further improvement of volume sensitivity. Mn^{2+} -doped CaTiO_3 and Fe^{3+} -doped SrTiO_3 samples were used to show the applicability of this resonator to dilute doped samples of oxides, but the results apply equally to any other dilute microcrystal. We have shown that the planar inverse anapole microresonator can be incorporated into existing spectrometers for easy deployment. This resonator design can easily couple to a microwave feedline and is scalable to higher frequencies without sacrificing ease of implementation, overcoming these limitations of previous microresonator designs. Easily applicable microresonator designs are necessary for routine studies of nanomaterials, for example, perovskite microcrystals and thin films, and biomacromolecular single crystals such as microcrystals of metalloenzymes. Owing to their ease of coupling with a microwave feedline and high power-to-field conversion efficiencies, these devices may also be potentially applied in EPR imaging modalities. Future work will include the construction of coupled arrays of these microresonator units—replacing a single unit with an array is expected to yield Q -factors approaching those of cavity resonators (>1000) at room temperature. We will also develop a variable-temperature probe with microfluidics to enable studies of liquid samples.

MATERIALS AND METHODS

Simulations

Finite element simulations were conducted using the electromagnetics module of COMSOL. The microresonator was modeled as a

perfectly conducting plane on a dielectric slab. The device model included the microstrip and the microresonator. The microstrip consisted of a dielectric with a ground plane on one face and a central conducting strip on the other face. The microresonator was modeled with the dielectric substrate directly in contact with the central conductor of the microstrip, and the metallic face pointing upward so that the metal film is separated from the central conductor of the microstrip by the dielectric of the microresonator. The dielectric constant of the microresonator substrate was set to 22 and that of the microstrip substrate was set to 3.55. A schematic of the complete model is provided in fig. S4, while fig. S5 shows the dimensions of features of the metallized layer.

Fabrication

The microresonators were fabricated on either LAO or LSAT substrates with a thickness of 500 μm and dielectric constants of 22 to 25. The substrates were first cleaned in piranha solution and then spin-coated with photoresist (LOR 10 prebaked at 175°C followed by SPR 220 prebaked at 115°C). The resonator layout was patterned into the photoresist using an ultraviolet laser (375 nm at 300 mJ/cm^2). The resist was developed using MIF300. The surface of the coated dielectric was then cleaned by reactive ion etching with oxygen plasma. Next, a 30-nm-thick film of Ti followed by a 500-nm-thick film of gold were deposited over the patterned photoresist using e-beam evaporation. Excess gold was removed by manual liftoff (soaked in Remover 1165 overnight). Last, a 50-nm layer of silicon nitride was deposited using plasma-enhanced chemical vapor deposition to protect the gold from abrasion.

Characterization of microresonators

The microresonators were coupled to a commercial RO4003 microstrip feedline. The microresonator was adhered to the microstrip using a small amount of silicone grease and was critically coupled to the microstrip by adjusting its position relative to the central conductor of the microstrip. The microstrip was terminated with a 50-ohm load. Coupling was monitored using a Keysight FieldFox vector network analyzer (VNA). Internal reflections from the coaxial cable were calibrated out by one-port short-open-load (SOL) calibration.

EPR spectroscopy

The critically coupled microresonator-microstrip device was affixed in a holder made of acrylonitrile butadiene styrene (ABS). To provide modulation of the static magnetic field, commercial air-core inductor coils were mounted on this holder and connected to the modulation amplifier in either a 10-GHz E580 Bruker spectrometer or NIST-built 35-GHz spectrometer. The microstrip was connected to the spectrometer bridge in each instrument using a coaxial cable. The microresonator-microstrip device was mounted on the ABS holder and placed in between the magnet poles of the spectrometer on an ABS post (fig. S11). In the EPR spectrometer operating at 10 GHz, the reference arm was kept on and the microwave frequency was locked at a value (around the dip observed on the VNA) that yielded an absorption lineshape. An automated procedure was run to match the response of the external modulation coils to the modulation amplitude settings in the EPR spectrometer. Here, the bandwidth of detection for CW spectra was defined as $(0.5 \times \text{conversion time})$. The NIST-built 35-GHz spectrometer operates without a reference arm (56). The resonant frequency of the 35-GHz microresonator-microstrip device was first identified on the VNA and then confirmed in the

spectrometer. In the 35-GHz system, we were able to apply a maximum modulation amplitude of only ≈ 0.1 mT due to internal settings. The modulation amplitude was determined from the linewidth of the EPR absorption line of a BDPA-benzene crystal. Here, the bandwidth was defined as $1/2\pi\tau$, where τ is the time constant.

Supporting information

A quantitative description of resonator sensitivity is provided in the Supplementary Materials. Also provided are additional simulations describing the inverse anapole mode, device dimensions, a phenomenological description of microstrip-microresonator coupling, and images of the microstrip-microresonator device placed in the spectrometer.

SUPPLEMENTARY MATERIALS

Supplementary material for this article is available at <http://advances.sciencemag.org/cgi/content/full/6/44/eabb0620/DC1>

REFERENCES AND NOTES

- P. Murali, Ferroelectric thin films for micro-sensors and actuators: A review. *J. Micromech. Microeng.* **10**, 136–146 (2000).
- D. G. Schlom, L.-Q. Chen, X. Pan, A. Schmehl, M. A. Zurbuchen, A thin film approach to engineering functionality into oxides. *J. Am. Ceram. Soc.* **91**, 2429–2454 (2008).
- J. W. Sidabras, J. Duan, M. Winkler, T. Happe, R. Hussein, A. Zouni, D. Suter, A. Schnegg, W. Lubitz, E. J. Reijerse, Extending electron paramagnetic resonance to nanoliter volume protein single crystals using a self-resonant microhelix. *Sci. Adv.* **5**, eaay1394 (2019).
- A. Bienfait, J. J. Pla, Y. Kubo, M. Stern, X. Zhou, C. C. Lo, C. D. Weis, T. Schenkel, M. L. W. Thewalt, D. Vion, D. Esteve, B. Julsgaard, K. Mølmer, J. J. L. Morton, P. Bertet, Reaching the quantum limit of sensitivity in electron spin resonance. *Nat. Nanotechnol.* **11**, 253–257 (2016).
- H. Zhao, Y. Duan, X. Sun, Synthesis and characterization of CaTiO_3 particles with controlled shape and size. *New J. Chem.* **37**, 986–991 (2013).
- A. S. Bhalla, R. Guo, R. Roy, The perovskite structure—A review of its role in ceramic science and technology. *Mater. Res. Innov.* **4**, 3–26 (2000).
- A. M. Glazer, Simple ways of determining perovskite structures. *Acta Crystallogr. Sect. A.* **31**, 756–762 (1975).
- N. W. Thomas, Crystal structure—physical property relationships in perovskites. *Acta Crystallogr. B* **45**, 337–344 (1989).
- F. Li, L. Jin, Z. Xu, S. Zhang, Electrostrictive effect in ferroelectrics: An alternative approach to improve piezoelectricity. *Appl. Phys. Rev.* **1**, 011103 (2014).
- S. Vasala, M. Karppinen, $\text{A}_2\text{B}^{\prime}\text{B}^{\prime\prime}\text{O}_6$ perovskites: A review. *Prog. Solid State Chem.* **43**, 1–36 (2015).
- R. A. De Souza, Oxygen diffusion in SrTiO_3 and related perovskite oxides. *Adv. Funct. Mater.* **25**, 6326–6342 (2015).
- F. Noll, W. Münch, I. Denk, J. Maier, SrTiO_3 as a prototype of a mixed conductor conductivities, oxygen diffusion and boundary effects. *Solid State Ion.* **86–88**, 711–717 (1996).
- R. A. Maier, C. A. Randall, Low-temperature ionic conductivity of an acceptor-doped perovskite: I. impedance of single-crystal SrTiO_3 . *J. Am. Ceram. Soc.* **99**, 3350–3359 (2016).
- K. A. Müller, T. W. Kool, *Properties of Perovskites and Other Oxides* (World Scientific, 2010).
- H. L. Tuller, S. R. Bishop, Point defects in oxides: Tailoring materials through defect engineering. *Annu. Rev. Mater. Res.* **41**, 369–398 (2011).
- E. S. Kirkpatrick, K. A. Müller, R. S. Rubins, Strong axial electron paramagnetic resonance spectrum of Fe^{3+} in SrTiO_3 due to nearest-neighbor charge compensation. *Phys. Rev.* **135**, A86–A90 (1964).
- J. C. Slonczewski, K. A. Müller, W. Berlinger, Dynamic Jahn-Teller effect of an impurity in a spontaneously distorted crystal. *Phys. Rev. B.* **1**, 3545–3551 (1970).
- T. von Waldkirch, K. A. Müller, W. Berlinger, Analysis of the $\text{Fe}^{3+} - \text{V}_\text{O}$ center in the tetragonal phase of SrTiO_3 . *Phys. Rev. B.* **5**, 4324–4334 (1972).
- R. A. Serway, W. Berlinger, K. A. Müller, R. W. Collins, Electron paramagnetic resonance of three manganese centers in reduced SrTiO_3 . *Phys. Rev. B.* **16**, 4761–4768 (1977).
- C. Boehme, K. Lips, The ultra-sensitive electrical detection of spin-Rabi oscillation at paramagnetic defects. *Phys. B Condens. Matter.* **376–377**, 930–935 (2006).
- L. S. Vlasenko, G. D. Watkins, Optical detection of electron paramagnetic resonance in room-temperature electron-irradiated ZnO. *Phys. Rev. B.* **71**, 125210 (2005).
- D. Rugar, R. Budakian, H. J. Mamin, B. W. Chui, Single spin detection by magnetic resonance force microscopy. *Nature* **430**, 329–332 (2004).
- J. P. Campbell, J. T. Ryan, P. R. Shrestha, Z. Liu, C. Vaz, J.-H. Kim, V. Georgiou, K. P. Cheung, Electron spin resonance scanning probe spectroscopy for ultrasensitive biochemical studies. *Anal. Chem.* **87**, 4910–4916 (2015).
- A. A. Basharin, V. Chuguevsky, N. Volsky, M. Kafesaki, E. N. Economou, Extremely high Q-factor metamaterials due to anapole excitation. *Phys. Rev. B.* **95**, 035104 (2017).
- T. Zentgraf, T. P. Meyrath, A. Seidel, S. Kaiser, H. Giessen, C. Rockstuhl, F. Lederer, Babinet's principle for optical frequency metamaterials and nanoantennas. *Phys. Rev. B.* **76**, 033407 (2007).
- A. Bitzer, A. Ortner, H. Merbold, T. Feurer, M. Walthert, Terahertz near-field microscopy of complementary planar metamaterials: Babinet's principle. *Opt. Express* **19**, 2537–2545 (2011).
- F. Falcone, T. Lopetegui, M. A. G. Laso, J. D. Baena, J. Bonache, M. Beruete, R. Marqués, F. Martin, M. Sorolla, Babinet principle applied to the design of metasurfaces and metamaterials. *Phys. Rev. Lett.* **93**, 197401 (2004).
- W. J. Wallace, R. H. Silsbee, Microstrip resonators for electron-spin resonance. *Rev. Sci. Instrum.* **62**, 1754–1766 (1991).
- G. Boero, M. Bouterfas, C. Massin, F. Vincent, P.-A. Besse, R. S. Popovic, A. Schweiger, Electron-spin resonance probe based on a 100 μm planar microcoil. *Rev. Sci. Instrum.* **74**, 4794–4798 (2003).
- R. Narkowicz, D. Suter, R. Stonies, Planar microresonators for EPR experiments. *J. Magn. Reson.* **175**, 275–284 (2005).
- S. Z. Kiss, A. M. Rostas, L. Heidinger, N. Spengler, M. V. Meissner, N. MacKinnon, E. Schleicher, S. Weber, J. G. Korvink, A microwave resonator integrated on a polymer microfluidic chip. *J. Magn. Reson.* **270**, 169–175 (2016).
- A. Blank, Y. Twig, Y. Ishay, Recent trends in high spin sensitivity magnetic resonance. *J. Magn. Reson.* **280**, 20–29 (2017).
- Y. Twig, E. Dikarov, A. Blank, Ultra miniature resonators for electron spin resonance: Sensitivity analysis, design and construction methods, and potential applications. *Mol. Phys.* **111**, 2674–2682 (2013).
- H. Malissa, D. I. Schuster, A. M. Tyryshkin, A. A. Houck, S. A. Lyon, Superconducting coplanar waveguide resonators for low temperature pulsed electron spin resonance spectroscopy. *Rev. Sci. Instrum.* **84**, 025116 (2013).
- N. Dayan, Y. Ishay, Y. Artzi, D. Cristea, E. Reijerse, P. Kuppasamy, A. Blank, Advanced surface resonators for electron spin resonance of single microcrystals. *Rev. Sci. Instrum.* **89**, 124707 (2018).
- J. A. Weil, J. R. Bolton, *Electron Paramagnetic Resonance* (John Wiley & Sons Inc., 2006).
- D. I. Hoult, R. E. Richards, The signal-to-noise ratio of the nuclear magnetic resonance experiment. *J. Magn. Reson.* (1969) **24**, 71–85 (1976).
- G. A. Rinard, R. W. Quine, R. Song, G. R. Eaton, S. S. Eaton, Absolute EPR spin echo and noise intensities. *J. Magn. Reson.* **140**, 69–83 (1999).
- E. J. Denlinger, Losses of microstrip lines. *IEEE Trans. Microw. Theory Tech.* **28**, 513–522 (1980).
- W. Froncisz, J. S. Hyde, The loop-gap resonator: A new microwave lumped circuit ESR sample structure. *J. Magn. Reson.* (1969) **47**, 515–521 (1982).
- E. Belohoubek, E. Denlinger, Loss considerations for microstrip resonators (short papers). *IEEE Trans. Microw. Theory Tech.* **23**, 522–526 (1975).
- R. L. Wood, W. Froncisz, J. S. Hyde, The loop-gap resonator. II. Controlled return flux three-loop, two-gap microwave resonators for ENDOR and ESR spectroscopy. *J. Magn. Reson.* (1969) **58**, 243–253 (1984).
- R. Narkowicz, D. Suter, Tuner and radiation shield for planar electron paramagnetic resonance microresonators. *Rev. Sci. Instrum.* **86**, 024701 (2015).
- O. B. Kobe, J. Chuma, R. Jamisola Jr., M. Chose, A review on quality factor enhanced on-chip microwave planar resonators. *Eng. Sci. Technol. Int. J.* **20**, 460–466 (2017).
- A. A. Basharin, M. Kafesaki, E. N. Economou, C. M. Soukoulis, V. A. Fedotov, V. Savinov, N. I. Zheludev, Dielectric metamaterials with toroidal dipolar response. *Phys. Rev. X* **5**, 011036 (2015).
- Y. Fan, Z. Wei, H. Li, H. Chen, C. M. Soukoulis, Low-loss and high-Q planar metamaterial with toroidal moment. *Phys. Rev. B* **87**, 115417 (2013).
- S. Yang, Z. Liu, L. Jin, W. Li, S. Zhang, J. Li, C. Gu, Surface plasmon polariton mediated multiple toroidal resonances in 3D folding metamaterials. *ACS Photonics* **4**, 2650–2658 (2017).
- Z. Liu, S. Du, A. Cui, Z. Li, Y. Fan, S. Chen, W. Li, J. Li, C. Gu, High-quality-factor mid-infrared toroidal excitation in folded 3D metamaterials. *Adv. Mater.* **29**, 1606298 (2017).
- A. Ahmadvand, B. Gerislioglu, Z. Ramezani, S. A. Ghoreishi, Attomolar detection of low-molecular weight antibiotics using midinfrared-resonant toroidal plasmonic metachip technology. *Phys. Rev. Appl.* **12**, 034018 (2019).
- C. Zuccaro, M. Winter, N. Klein, K. Urban, Microwave absorption in single crystals of lanthanum aluminate. *J. Appl. Phys.* **82**, 5695–5704 (1997).
- C. Zuccaro, I. Ghosh, K. Urban, N. Klein, S. Penn, N. M. Alford, Materials for HTS-shielded dielectric resonators. *IEEE Trans. Applied Supercond.* **7**, 3715–3718 (1997).
- G. R. Eaton, S. S. Eaton, D. P. Barr, R. T. Weber, *Quantitative EPR* (Springer Vienna, 2010).
- C. Altenbach, W. Froncisz, R. Hemker, H. Mchaourab, W. L. Hubbell, Accessibility of nitroxide side chains: Absolute heisenberg exchange rates from power saturation EPR. *Biophys. J.* **89**, 2103–2112 (2005).

54. C. Rodenbücher, M. Luysberg, A. Schwedt, V. Havel, F. Gunkel, J. Mayer, R. Waser, Homogeneity and variation of donor doping in Verneuil-grown SrTiO₃:Nb single crystals. *Sci. Rep.* **6**, 32250 (2016).
55. R. A. Maier, K. F. Garrity, M. P. Donohue, A. Ozarowski, I. Levin, Effects of octahedral tilting on the site of substitution of manganese in CaTiO₃. *SSRN Electron. J.* (2020).
56. A. Band, M. P. Donohue, B. Epel, S. Madhu, V. A. Szalai, Integration of a versatile bridge concept in a 34 GHz pulsed/CW EPR spectrometer. *J. Magn. Reson.* **288**, 28–36 (2018).
57. B. Elschner, Ch. P. Poole Jr., Electron-Spin-Resonance, 2nd Edition, A Comprehensive Treatise on Experimental Techniques, John Wiley and Sons, New York, Chichester, Brisbane, Toronto, Singapore 1983. 780 Seiten, Preis: £ 61. *Berichte Bunsenges. Für Phys. Chem.* **87**, 1230 (1983).

Acknowledgments

Funding: N.A. and A.A. acknowledge partial support under the Cooperative Research Agreement between the University of Maryland and the National Institute of Standards and Technology Physical Measurement Laboratory, Award 70NANB14H209, through the University of Maryland. G. Holland and S. Blankenship at NIST are acknowledged for assistance in design and machining of microstrip assembly holders. D. Rutter and A. Band (deceased) are acknowledged for electrical engineering support, specifically for modulation coil characterization, and testing. Certain commercial equipment, instruments, or materials are identified in this paper to specify the experimental procedure adequately. This identification is not intended to imply recommendation or endorsement by the National Institute of Standards and Technology nor is it intended to imply that the materials or equipment identified are necessarily the best available for the purpose. **Author contributions:** All authors

contributed to the design of experiments, interpretation of data, and writing of the manuscript. N.A. and V.S. were involved in all stages, including conception of the idea, designing experiments, conducting measurements, and interpretation of data. Simulations were performed by N.A. and A.A. Resonator fabrication was conducted by N.A. N.A., R.D.M., and V.S. designed the microresonator-microstrip devices. N.A., J.C., P.S., and V.S. conducted EPR spectroscopic measurements. R.M. provided characterized samples of dilute perovskites. **Competing interests:** All authors declare that they have no competing interests. NIST filed the U.S. provisional patent application titled “Planar Inverse Anapole Microresonators for Inductive Detection Electron Paramagnetic Resonance Spectroscopy” (serial number 62/982879) on February 28, 2020. N.A., A.A., and V.S. are also on the patent application. University of Maryland, College Park filed the same provisional patent application with the same authors under serial number 63/05581 on July 23, 2020. These patent applications may be impacted by the present publication. **Data and materials availability:** All data needed to evaluate the conclusions in the paper are present in the paper and/or the Supplementary Materials. Additional data related to this paper may be requested from the authors.

Submitted 27 January 2020
Accepted 14 September 2020
Published 28 October 2020
10.1126/sciadv.abb0620

Citation: N. Abhyankar, A. Agrawal, P. Shrestha, R. Maier, R. D. McMichael, J. Campbell, V. Szalai, Scalable microresonators for room-temperature detection of electron spin resonance from dilute, sub-nanoliter volume solids. *Sci. Adv.* **6**, eabb0620 (2020).